Optical Pushing: A tool for parallelized biomolecule manipulation

Gerrit Sitters[‡1], *Niels Laurens*[‡1*], *Emile J de Rijk*[1,], *Holger Kress*[2,3], *Erwin JG Peterman*[1], *Gijs JL Wuite1*[1,*]

1. Department of Physics and Astronomy and Laser Centre, VU University, The Netherlands

2. Experimental Physics I, University of Bayreuth, Bayreuth, Germany

3. Department of Applied Physics, Eindhoven University of Technology, Eindhoven, The Netherlands

Supplementary information

Proteins and buffers. The FokI protein was purified was purified from an over-producing strain of E-coli. DNA binding experiments were performed in a 20mM Tris-acetatie (pH 7.8), 50 mM potassium acetate, 2 mM $CaCl_2$ and I mM DTT buffer. Experiments on naked DNA were conducted in PBS.

The analytical model. To determine the exerted force on tethered molecules it is important to understand the motion of the system. Apart from translational Brownian motion the microspheres also experiences rotational Brownian motion causing them to swivel around the attachment point as shown schematically for one dimension in **Supplementary Fig. 2a,b**. Existing force calibration methods for tethered microspheres, which are used for instance for MT, are not directly applicable to our system. Microsphere rotation is neglected in these models because of the fixed alignment of the paramagnetic microsphere with the external magnetic field[1]. Neglected microsphere rotation leads to an underestimation of the applied force (**Supplementary Fig. 3**). We therefore derived a power spectrum for the microspheres motion parallel to the surface using the Langevin equation for both the translation as the rotation[2,3]:

$$m\frac{d\vec{v}}{dt} = \vec{F}_{brown}(t) - \vec{\gamma}\cdot\vec{v}(t) + \vec{F}_{ext}(t)$$
$$I\frac{d\vec{\omega}}{dt} = \vec{T}_{brown}(t) - \vec{\beta}\cdot\vec{\omega}(t) + \vec{T}_{ext}(t)\,, \qquad (5)$$

where $\vec{v}$ and $\vec{\omega}$ are respectively the translational and angular velocity, m is the particle mass and I is the moment of inertia of the particle. The forces due to the laser, the tether, the surface, buoyancy and

gravity are included in the external force term $\vec{F}_{ext}$ and are described in detail bellow. Equations (5) account for the increased viscous drag near the surface, using Faxen's law for both the translation and rotation coefficients $\vec{\gamma}$ and $\vec{\beta}$ (see section surface effects, equations (12)). The external torque $\vec{T}_{ext}$ results from the cross product of the vector between the microsphere center and the DNA attachment point $\vec{R}$ and the DNA force $\vec{F}_{DNA}$ (**Supplementary Fig. 2b**). $\vec{F}_{brown}$ and $\vec{T}_{brown}$ are the fluctuating thermal force and torque. The amplitude of these terms are described by the fluctuation-dissipation theorem and are Gaussian distributed with the following statistical properties[4]:

$$\langle F_{brown}(t)\rangle = 0$$
$$\langle T_{brown}(t)\rangle = 0$$

$$\langle F_{brown}(t')F_{brown}(t'+t)\rangle = 2\gamma k_B T\delta(t)$$

$$\langle T_{brown}(t')T_{brown}(t'+t)\rangle = 2\beta k_B T\delta(t). \qquad (6)$$

With $\delta(t)$ the Dirac delta function. The inertial terms in equations .5) are neglected since the Reynolds number is sufficiently low. For microspheres in the micro range the Reynolds number is in the order of $1\cdot 10^{-3}$ at room temperature (**Supplementary Table 1**).

To simplify calculations we assume a laser force $F_{laser} \gg F_{brown}$, leading to small angles of θ, α, φ, β and ξ (**Supplementary Fig. 2a,b**). The DNA-microsphere system is in equilibrium when the DNA and vector $\vec{R}$ are aligned with the z axis. If the system is pulled out of equilibrium due to Brownian fluctuations the DNA and the laser force will tend to force the microsphere back into equilibrium:

$$F_{restoring,x} = F_{DNA}\cdot sin\theta$$

$$T_{restoring,y} = |R|\cdot|F_{DNA}|\cdot sin\beta. \qquad (7)$$

Assuming that $|F_{DNA}| = |F_{laser}|$ (for $\theta \ll 1$), $|\varphi| + \alpha + \xi \ll 1$ and $x_{cm} = x_{DNA} + R\varphi$ (see **Supplementary Figure 2a,b** we derive the following linearized versions of equations (7):

$$\beta = \pi - (\alpha+\varphi) - \xi$$

$$\alpha = \tan^{-1}\frac{x_{cm}}{z} \approx \frac{x_{cm}}{z}$$

$$(z-R)\,\xi \approx R(\alpha+\varphi) \rightarrow \xi \approx \frac{R\alpha}{z-R} + \frac{R|\varphi|}{z-R} \approx \frac{Rx_{cm}}{z^2-zR} + \frac{R|\varphi|}{z-R}$$

$$F_{restoring,x} = F_{laser}\cdot\frac{x_{DNA}}{z-R} = F_{laser}\cdot\frac{x_c - R\varphi}{z-R}$$

$$T_{restoring} = |R|\cdot|F_{laser}|\cdot sin(\pi - |\varphi| - \alpha - \xi) = |R|\cdot|F_{laser}|\cdot sin(|\varphi| + \alpha + \xi)$$
$$= |R|\cdot|F_{laser}|\cdot\left(|\varphi| + \frac{x_{cm}}{z} + \frac{Rx_{cm}}{z^2-zR} + \frac{R|\varphi|}{z-R}\right). \qquad (8)$$

See **Supplementary Figure 2c** how they compare to the non-linearized force and torque (using the numerical simulations described below). To calculate the power spectrum of equations (5) we

implement the linearized restoring force and torque as the external force and torque in these equations and calculate the Fourier transform, with $\tilde{x}(\omega) = \int_{-\infty}^{\infty} x(t)e^{-i\omega t}dt$. Note that surface, buoyancy and gravity forces are neglected:

$$\tilde{F}_{brown} = i\omega\gamma\tilde{x}_{cm} - \frac{F_{laser}}{z-R}(\tilde{x}_{cm} - R\tilde{\varphi})$$

$$\tilde{T}_{brown} = i\omega\beta\tilde{\varphi} - RF_{laser}\left(|\tilde{\varphi}| + \frac{\tilde{x}_{cm}}{z} + \frac{R\tilde{x}_{cm}}{z^2-zR} + \frac{R|\widetilde{\varphi}|}{z-R}\right). \quad (9)$$

From these equations we derive the power spectrum $P(f) \equiv \langle\tilde{x}_{cm}\tilde{x}_{cm}^*\rangle$, with the frequency f (* denotes the complex conjugate), using the relations $\langle\tilde{F}_{brown}^2\rangle = 2\gamma k_B T$ and $\langle\tilde{T}_{brown}^2\rangle = 2\beta k_B T$:

$$P(f) = 2k_b T\frac{(\beta+\gamma\langle z\rangle^2)R^2F^2+(\langle z\rangle-R)^2\beta^2\gamma(2\pi f)^2}{\left((R-\langle z\rangle)\beta\gamma(2\pi f)^2+RF^2\right)^2+(2(R\gamma\langle z\rangle-\beta)F\pi f)^2}. \quad (10)$$

Note that the equation (10) reduces to the power spectrum of magnetic tweezers when $\beta = 0$ (neglecting rotation) is implemented (equation 4).

Numerical simulations. To validate the assumptions made in the derivation of the analytical power spectrum we also simulated microsphere movement. The microsphere equation of translation and rotation was solved numerically using the following equations:

$$\vec{x}_{n+1} = \vec{x}_n + \vec{\gamma}^{-1}\cdot\left(\vec{F}_{ext} + \vec{F}_{brown}\right)\Delta t$$

$$\vec{\varphi}_{n+1} = \vec{\varphi}_n + \vec{\beta}^{-1}\cdot\left(\vec{T}_{ext} + \vec{T}_{brown}\right)\Delta t, \quad (11)$$

where $\vec{x}_n$ and $\vec{x}_{n+1}$ is the microspheres three dimensional position at the step n and $n+1$ of the simulation respectively. $\vec{\varphi}_n$ and $\vec{\varphi}_{n+1}$ denote the microspheres orientation. In order to simulate the microspheres trajectory we implemented an initial microsphere position and rotation, after which successive positions and rotations were calculated using equations (11). The Brownian force and torque terms were drawn from Gaussian distributions that suffice equations (6) where the Dirac delta distribution was set to $\delta(t) = 1/\Delta t$, with Δt the time step of the simulation for which we typically used 10^{-5}s. Decreasing Δt did not affect the statistical properties (such as the RMS, correlation time and power spectra) of the simulated traces.

Surface effects. Equations (5) account for the increased viscous drag near the surface, using Faxen's law for both the translation and rotation coefficients for the parallel and perpendicular direction relative to the surface[5]:

$$\gamma_x = \gamma_y = \frac{\gamma_0}{1 - \frac{9}{16}\left(\frac{R}{z}\right) + \frac{1}{8}\left(\frac{R}{z}\right)^3 - \frac{45}{256}\left(\frac{R}{z}\right)^4 - \frac{1}{16}\left(\frac{R}{z}\right)^5}$$

$$\gamma_z = \frac{\gamma_0}{1 - \frac{9}{8}\left(\frac{R}{z}\right) + \frac{1}{2}\left(\frac{R}{z}\right)^3 - \frac{57}{100}\left(\frac{R}{z}\right)^4 + \frac{1}{5}\left(\frac{R}{z}\right)^5 + \frac{7}{200}\left(\frac{R}{z}\right)^{11} - \frac{1}{25}\left(\frac{R}{z}\right)^{12}}$$

$$\beta_x = \beta_y = \frac{\beta_0}{1 - \frac{1}{8}\left(\frac{R}{z}\right)^3}$$

$$\beta_z = \frac{\beta_0}{1 - \frac{5}{16}\left(\frac{R}{z}\right)^3 + \frac{15}{256}\left(\frac{R}{z}\right)^6} \quad (12)$$

where γ_0 and β_0 are respectively the translational and rotational drag coefficients in bulk and are defined as $\gamma_0 = 6\pi\eta R$ and $\beta_0 = 8\pi\eta R^3$, with R is the microspheres radius and z is the microsphere center-surface separation in the axial direction and η representing the dynamic viscosity.

External forces. The external forces that are implemented in our numerical simulation are the laser force $\vec{F}_{laser}$, the force of the DNA $\vec{F}_{DNA}$, the force of the surface $\vec{F}_{surface}$, the buoyancy force $\vec{F}_{buoyancy}$ and the gravitational force $\vec{F}_{gravity}$. The laser force is implemented as a constant force in z direction and is set manually:

$$\vec{F}_{laser} = F_{laser}\hat{z} \quad (13)$$

The force of the DNA is calculated with the extensible worm like chain model[6]:

$$\vec{F}_{DNA} = -\left(\frac{k_B T}{L_p}\right)\left[\frac{1}{4}\left(1 - \frac{\vec{a}}{L_c} + \frac{\vec{F}_{DNA}}{S}\right)^{-2} - \frac{1}{4} + \frac{\vec{a}}{L_c} - \frac{\vec{F}_{DNA}}{S}\right], \quad (14)$$

with L_p, L_c and S respectively the persistence length, the contour length and the stretch modules of DNA (**Supplementary Table 1**). The vector $\vec{a} = (x_{DNA}, y_{DNA}, z_{DNA})$ points from the DNA-surface attachment point towards the DNA-microsphere attachment point. The surface force results from the electrostatic interaction between microsphere and surface[7]:

$$\vec{F}_{surface} = 4\pi\epsilon_W\epsilon_0\psi_0^2 R e^{-(z-R)/l}\hat{z}\,, \quad (15)$$

with ϵ_W and ϵ_0 respectively the permittivity of water and vacuum, ψ_0 the effective surface potential, R the microsphere radius, z the axial distance between surface and microsphere center and l the Debye screening length. The buoyancy and gravity forces are implemented as follows:

$$\vec{F}_{buoyancy} + \vec{F}_{gravity} = \frac{4}{3}\pi R^3 g(\rho_{med} - \rho_{bead})\hat{z}, \quad (16)$$

with g the gravitational constant, ρ_{med} the density of water and ρ_{bead} the density of the microsphere. See the supplementary information for the parameters used.

Mie calculations. Radiation pressure exerted on a spherical particle by a beam of light is calculated using Mie theory[8]. The laser force is expressed in terms of the extinction coefficient C_{ext}, the scattering cross section C_{sca} and the average cosine of the scattering angles $\langle cos\theta \rangle$:

$$F_{laser} = \frac{n_m I}{c}(C_{ext} - C_{sca}\langle cos\theta \rangle), \quad (17)$$

with n_m the refractive index of the surrounding medium, I the laser intensity and c the speed of light. C_{ext}, C_{sca} and $\langle cos\theta \rangle$ are expressed by:

$$C_{sca} = \frac{2}{x^2}\sum_{n=1}^{\infty}(2n+1)(|a_n|^2 + |b_n|^2),$$

$$C_{ext} = \frac{2}{x^2}\sum_{n=1}^{\infty}(2n+1)Re\{a_n + b_n\},$$

$$\langle cos\theta \rangle = \frac{4\pi R^2}{x^2 C_{sca}}\sum_{n=1}^{\infty}\left[\frac{n(n+2)}{n+1}Re\{a_n a_{n+1}^* + b_n b_{n+1}^*\} + \frac{2n+1}{n(n+1)}Re\{a_n b_n^*\}\right], \quad (18)$$

where $x = 2\pi R/\lambda$, R is the particle radius, λ is the wavelength of the light in the surrounding medium and the asterisk denotes complex conjugation. a_n and $b_n$are classical Mie coefficients depending on the particle size and material. The calculation of these coefficients is done according to Bohren et al[8]. See the **Supplementary Table 1** for the material parameters.

Once a_n and b_n are calculated the equation above are used to derive the laser force acting on the particles numerically. To decrease computation times, the summations are terminated after $n_{max=}x + 4x^{1/3} + 2$. This amount a terms has proven to be sufficient to calculate a_n and b_n correctly[8].

Loading rates. Laser powers and therefore the laser forces on the microspheres can be altered with a frequency in the 100Mhz regime using AOMs. The tension of the DNA will respond much slower due to the viscous drag of the microsphere. To calculate the response time of the system the following equation of motion for the microsphere is solved (inertia is neglected):

$$F_{laser}(t) - \gamma\dot{x}(t) - kx(t) = 0, \quad (19)$$

with $\dot{x}$ the time derivative of the position x and k the stiffness of the DNA. If we assume that both the laser force and the stiffness of the DNA are constant, the solution of the equation of motion is $(t) = \frac{F_{laser}}{k}\left(1 - e^{-\frac{k}{\gamma}t}\right)$. The response time of the system is thus proportional to $\frac{\gamma}{k}$. **Supplementary Figure 7a** shows that the typical switching time lies in the order of 100 µs for 4µm microsphere in diameter and a DNA stiffness of 2,000 $pN/\mu m$ (enthalpic regime of DNA with L_c=0.5 µm). Linear force ramps exerted on the DNA can be achieved below the response time of the system if a linearly increasing laser force is applied with an initial offset (**Supplementary Fig. 7b**). The initial laser offset that should be applied to create a linear loading rate on the DNA is proportional to the height of the loading rate. This limits the force range for high loading rates. **Supplementary Figure 7b** shows that it is possible to apply a loading rate of $10^6\ pN\ /\ s$ over 50 % of the total force range. This range increases to 95 % for a loading rate of $10^5\ pN\ /\ s$. The smallest achievable loading rate using OP is limited by the laser power stability, which typically fluctuates 1 % over 4 hours (IPG laser spec. sheet). To achieve a loading rate that is linear within an accuracy of 10 %, the loading rate should at least be ten times larger than the rate of the laser power fluctuations. This results in a minimal loading rate of $\frac{F_{laser,max}}{1440s} \sim 3 \cdot 10^{-2}\ pN\ /\ s$ for a maximum loading force of 40 pN. The power fluctuations of the laser can be reduced using a feedback loop to control the laser power. Laser intensity stabilizers can attenuate the noise by a factor

of 400.[9] This decreases the minimum force ramp to $\sim 1 \cdot 10^{-4}\ pN\ /\ s$ for a maximum loading force of 40 pN.

Force calibration using RMS motion. To calibrate the forces on the small beads (ϕ 440 nm) in the entropic regime (<0.1 pN) we used our numerical simulations (see Figure 3c). To determine the calibration factor we calculated the root mean square difference ($RMSD = \sqrt{\frac{\sum_N (RMS_{meas} - RMS_{sim})^2}{N}}$) between the simulated and measured data points as a function of calibration factor (see Supplementary Figure 11)

Sample heating. Since a high intensity laser is used to apply forces in the sample, it is important to quantify any potentially harmful heating effects. It has been shown that in an optical tweezers experiment, where the light ($100\mathrm{mW}$ at $1064\mathrm{nm}$) is tightly focused, there is a small temperature increase of approximately 0.8 K in the focus, which does not damage the biological sample[10]. The laser powers used in the Optical Pushing instrument is two orders of magnitude higher (up to 15W), but the laser beam is not focused in the sample. Therefore it is of interest to calculate the heating, using the theoretical model that is derived by Peterman et al. [10] and applying it to a collimated beam.

Laser induced heating is mainly determined by the heating of the buffer in the sample and has a maximum in the center of the flow cell. A solvent's ability to absorb a plane wave of light with intensity I travelling in the x-direction through the solvent is determined by its extinction coefficient γ, which is translated to the heat per volume, Q, generated per time in the solvent:

$$I(x) = I_0 e^{-\gamma x}, \tag{19}$$

$$\frac{dQ}{dt} = -\frac{dI}{dx} = \gamma I\ . \tag{20}$$

This generated heat will be dissipated by a heat flow J that is calculated using the local differential equation:

$$J\left(\vec{r}\right) = -C\nabla\left(\Delta T\left(\vec{r}\right)\right), \tag{21}$$

where C is the thermal conductivity of the solvent and $\Delta T(\vec{r})$ is the temperature deviation from ambient temperature due to heating at position $\vec{r}$. In a steady state solution the heat generated is in equilibrium with the amount of heat dissipated: $\nabla J = dQ/dt$, leading to (using equations (20) and(21)):

$$\nabla^2\left(\Delta T\left(\vec{r}\right)\right) = -\frac{\gamma}{C} I\left(\vec{r}\right). \tag{22}$$

Solving equation 22 for $r = 0$ will give the temperature increase in the center of the laser beam. To solve equation 22 the Green's function is used that satisfies:

$$\nabla^2 G\left(\vec{r}, \vec{r}\,'\right) = \delta^3\left(\vec{r}, \vec{r}\,'\right), \tag{23}$$

with δ the Dirac delta function. Setting the argument $\vec{r}'$ to zero and implementing the boundary condition of $G = 0$ at a radial distance S leads to:

$$G(r) = -\frac{1}{4\pi}\left(\frac{1}{r} - \frac{1}{S}\right). \tag{24}$$

This boundary condition represents the quartz surface that is present at a distance S and acts as a heat sink. To calculate the maximum temperature in the center of the flow cell, an S of $50\ \mu\mathrm{m}$ is taken into account. In terms of $G(r)$, the solution of equation (22) at the center of the laser beam is:

$$\Delta T(0) = \int G(r)\left(-\frac{\gamma}{C} I(r)\right) dV\ . \tag{25}$$

Setting $dV = r^2 dr d\Omega$ and implementing $G(r)$ and $I(r)$, leads to:

$$\Delta T = \frac{\gamma I_{tot}}{8\pi^2 C\beta^2} \int_{r<R} \left(\frac{1}{r} - \frac{1}{S}\right) e^{\frac{-r^2}{2\beta^2}} r^2 dr d\Omega \quad = \quad \frac{\gamma I_{tot}}{4\pi C\beta^2} \int_0^R \left(\frac{1}{r} - \frac{1}{S}\right) e^{\frac{-r^2}{2\beta^2}} r^2 dr\ , \tag{26}$$

where I_{tot} is the total laser intensity and $\beta = FWHM/2\sqrt{2ln2}$. This integral is solved numerically, which results in a heating of approximately $0.72\ \mathrm{K}$ at the center of the flow chamber when the following parameters are implemented: $\alpha = 14.2\mathrm{m}^{-1}$ (extinction coefficient of water), $C = 0.6\ \mathrm{W/mK}$ (thermal conductivity of water) and $I_{tot} = 1\ \mathrm{W}$. Note that the temperature increase at the assay, which is close to the surface, is less due to the high thermal conductivity of quartz

Parameter	Variable	Value (for $1\mu m$ polystyrene microsphere at 21°C)
Viscosity of medium	η	1.00 mPa s
Refractive index medium at 1070 nm	n_{med}	$1.32 + 10^{-6}i$
Refractive index polystyrene at 1070 nm	n_{poly}	$1.58 + 0i$
Refractive index melamine at 1070 nm	n_{mel}	$1.68 + 0i$
Refractive index titania at 1070 nm	n_{tit}	$2.50 + 0i$
Refractive index gold at 1070 nm	n_{gold}	$0.27 + 7.15i$
Density polystyrene	ρ_{poly}	1.05 g cm^{-3}
Density melamine	ρ_{mel}	1.57 g cm^{-3}
Density titania	ρ_{tit}	4.23 g cm^{-3}
Density gold	ρ_{gold}	19.3 g cm^{-3}
Viscous drag of microsphere	$\gamma = 6\pi R\eta$	9.42 pN s μm^{-1}
Average thermal microsphere velocity	$v_{th} = \sqrt{k_B T/m}$	2.71 mm s^{-1}
Reynolds number	$Re = Rv_{th}\rho/\eta$	$1.4 \cdot 10^{-3}$
Absolute permittivity of water	$\epsilon_0\epsilon_W$	$70.832 \cdot 10^{-13}\ \mathrm{Fm}^{-1}$
Effective surface potential	ψ_0	5 mV
Debye screening length	l	10 nm

Persistence length of DNA	L_p	50 nm
Stretch modulus of DNA	S	1500 pN

Supplementary Table 1: parameters used for calculations.

Supplementary figures

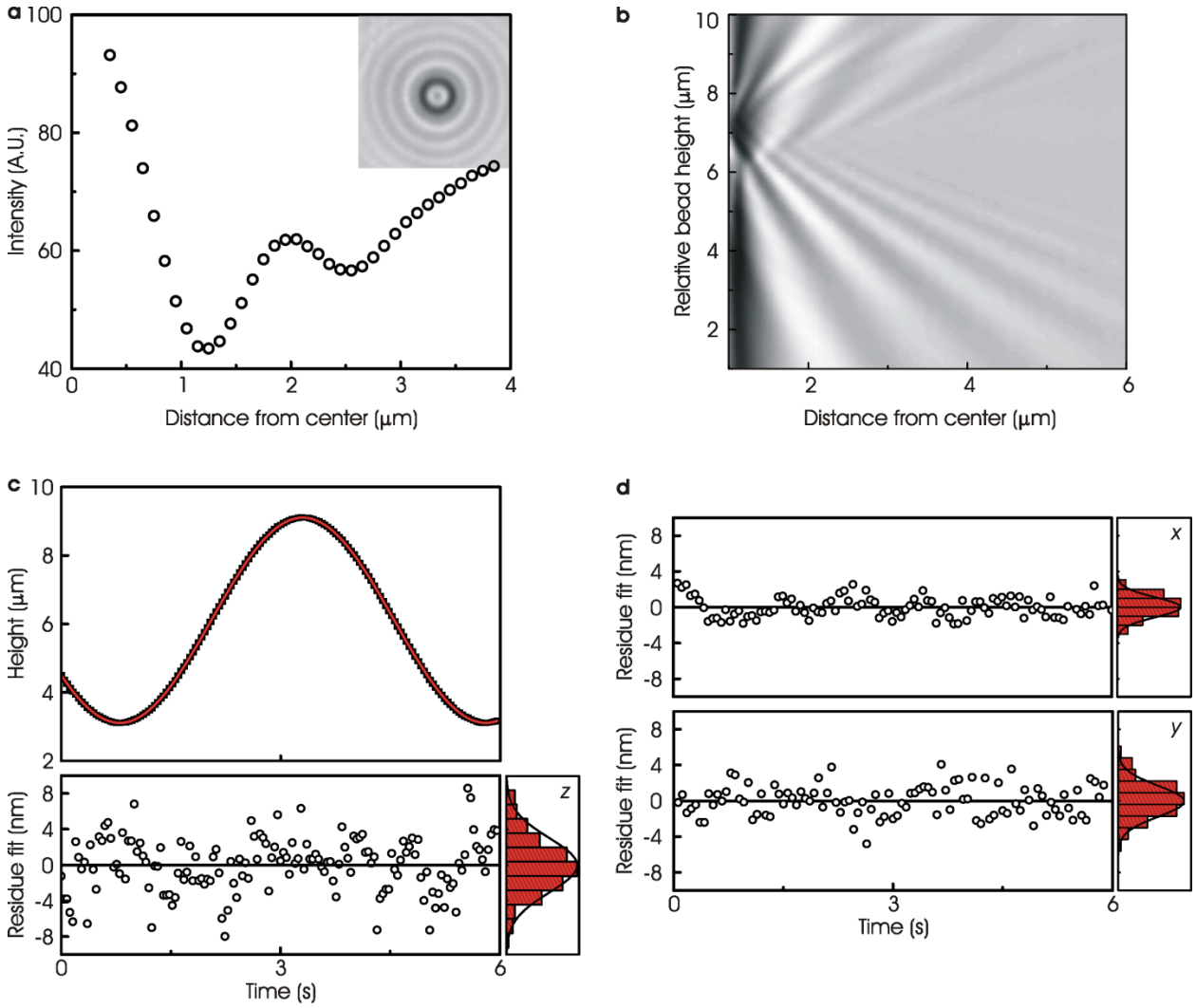

Supplementary Figure 1 | *Relative height determination of a microsphere using a look up table (LUT).* ***a.*** *Images of the microsphere (inset) are converted to a radial profile. Radial profiles of 6 images are averaged and binned over 100 nm. The radial profile is measured as a function of the microsphere height, using the piezo stage to control the height. (**b**) Stack of radial profiles as a function of the relative microsphere height. During a measurement the microspheres radial profile is compared to the radial profiles in the LUT to obtain the microspheres height.* ***c.*** *To determine the accuracy of our microsphere*

tracking in z (at 25 Hz) we measured the height of a stuck microsphere (2.1 um diameter) that is moved up and down in a sinusoidal manner using the piezo stage. The standard deviation of the residues from the sinusoidal fit of the height data is 4 nm, which is the accuracy we achieve in z. ***d.*** *The residues in the x- and y-dimension, determined in the same way as in* ***c*** *but moving the piezo stage in respectively x and y. In both these dimensions we achieve an accuracy of approximately 2nm (at 25 Hz).*

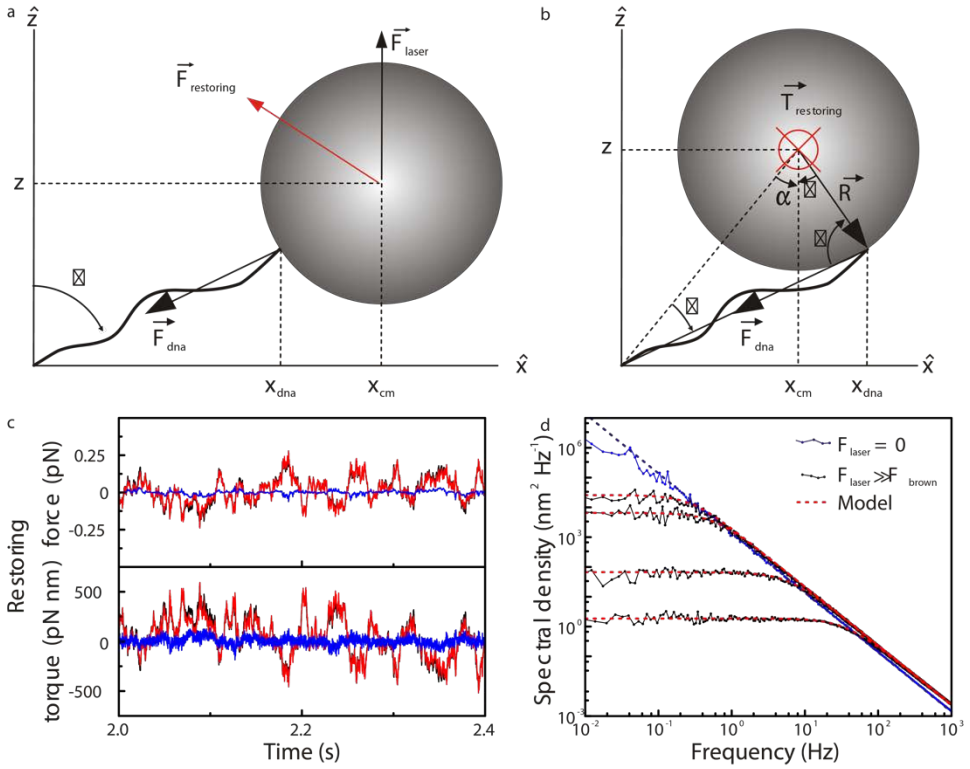

Supplementary Figure 2 | *Schematic overview of a DNA tether pushed out of its equilibrium position by the Brownian force.* ***a****. The displacement due to the Brownian motion leads to a small angle ϑ, giving rise to a restoring force. Note that there is also a difference between the observed center of the microsphere and the real attachment point of the DNA.* ***b****. The displacement and rotation of the microsphere (ϕ) lead to a different anchor point position of the DNA and to a restoring torque acting on the center of the microsphere. The angles α, β, ξ are introduced to assist the calculations.* ***c****. Comparison of the restoring torque and force for the linearized (red) and full model (black). The residuals (blue) are symmetrical and have a standard deviation of 0.01 pN and 26 pN·nm for the force and torque respectively.* ***d****. Power spectra of the simulated data sets and plots of the analytical model using the same parameters (ϕ 4.26 μm, 1.1 kbp DNA). The spectra from top to bottom are simulated and calculated using applied forces of 0 pN, 0.5*

pN, 1 pN, 10 pN, 60 pN for the spectra from top to bottom. The spectrum and plot in the absence of force is given in blue for reference.

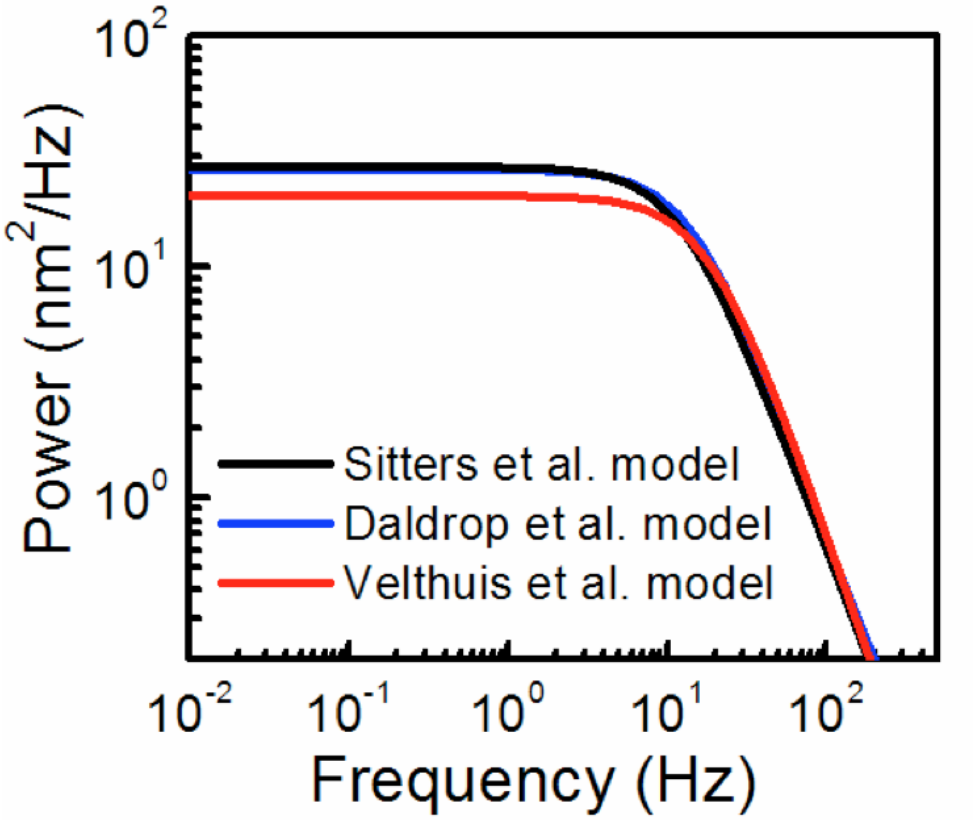

Supplementary Figure 3 | *Calculated power spectra of the Daldrop et al., Velthuis et al. and the model used in the paper for for a microsphere that is 3 µm in diameter, a DNA molecule with a contour length of 0.3 µm and an exerted force of 10 pN. The graph shows good agreement between the model used in the paper and the Daldrop model. The power spectrum calculated with the Velthuis model differs significantly below the cut of frequency.*

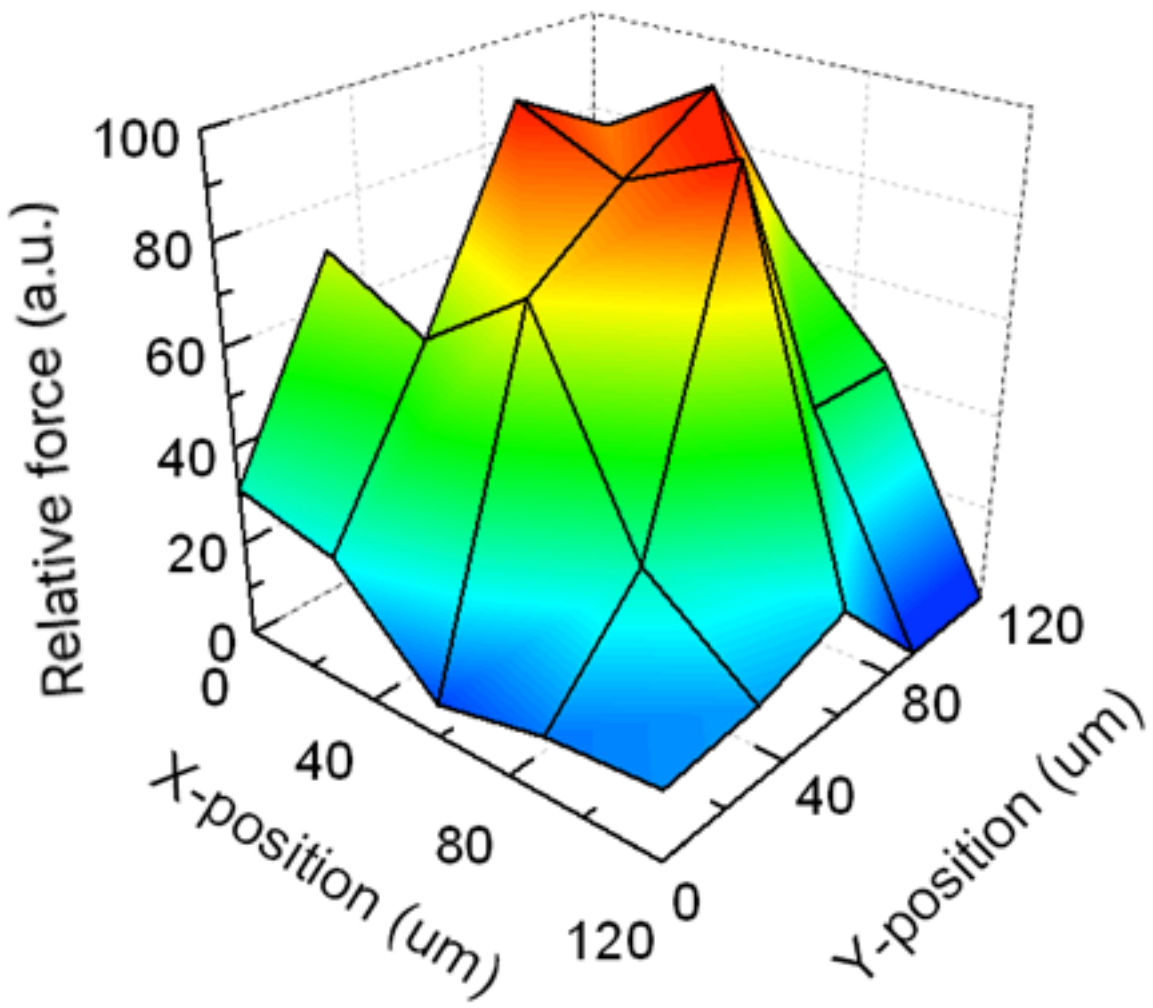

Supplementary Figure 4 | *The measured force profile within a field of view on the camera. This plot is acquired by measuring the force on the same bead at 25 different locations within the field of view using the same laser power. The profile has a FWHM of* 74 ± 9 nm (using a 2D Gaussian fit).

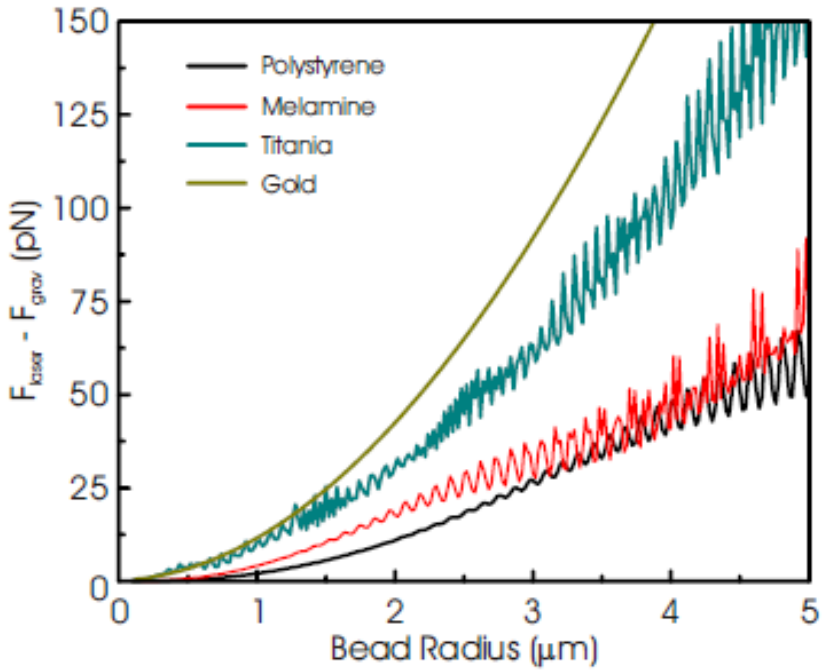

Supplementary Figure 5 | *The calculated optical pushing force for different materials using Mie theory (gravity force is substracted). In general materials with a higher refractive index experience a bigger force using the same intensity. Calculations were performed for particles in the center of a 1064nm, 100μm FWHM and 8W laser.*

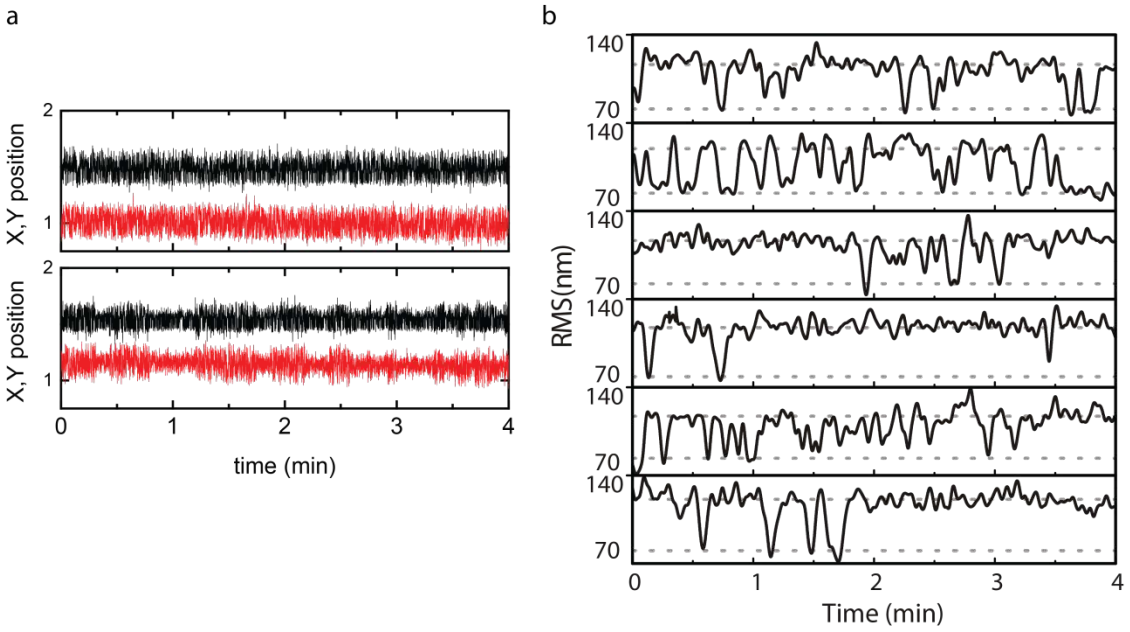

Supplementary Figure 6 | ***a***. *Raw data traces of the X (black) and Y (red) position of a tethered microsphere (ϕ 440 nm) in the absence (top) and presence (bottom) of the FokI restriction enzyme under a constant force of ~10 fN. If FokI is present, looping behavior is observed resulting in smaller bead motion in both dimensions.* ***b***. *Root mean square (RMS) traces (2s time window) of simultaneous measured microspheres under constant force of ~ 10 fN, show clear looping behavior (indicated by the dashed lines) in the presence of the FokI restriction enzyme. The length of the DNA in the unlooped state is 180 nm and I the looped state 115 nm.*

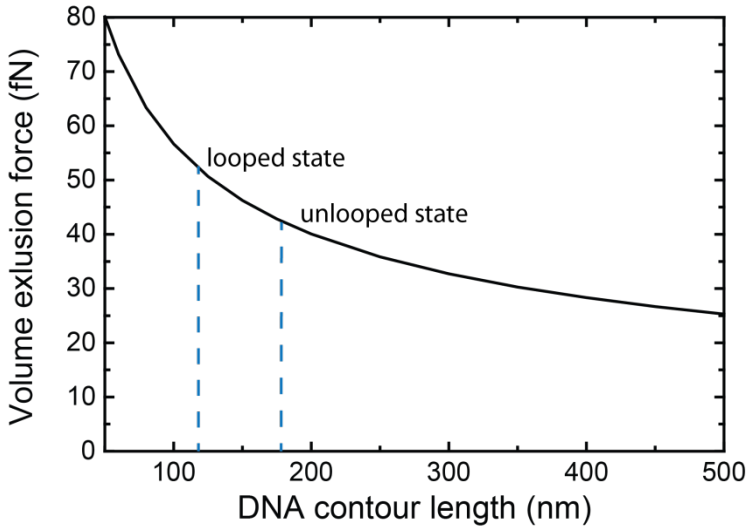

Supplementary Figure 7 | *The calculated volume exclusion force of a tethered microsphere (ϕ 440 nm) as a function of DNA contour length*[11]*. This plot shows that the volume exclusion force decreases less than 10 fN going from looped to unlooped state.*

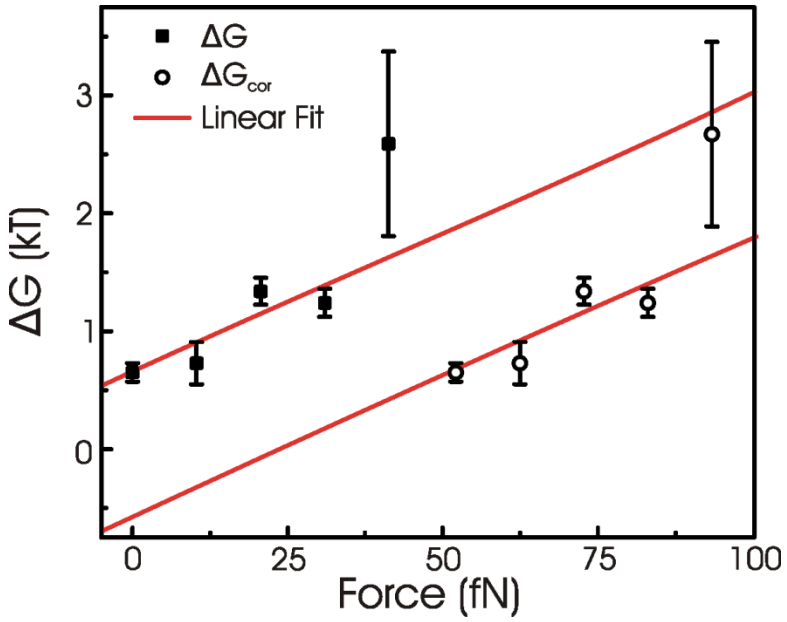

Supplementary Figure 8 | *Calculated free energy change ΔG at different forces for both the uncorrected and corrected forces (volume exclusion force taken into account). The linear fit is used to determine the standard free energy change* ΔG^0.

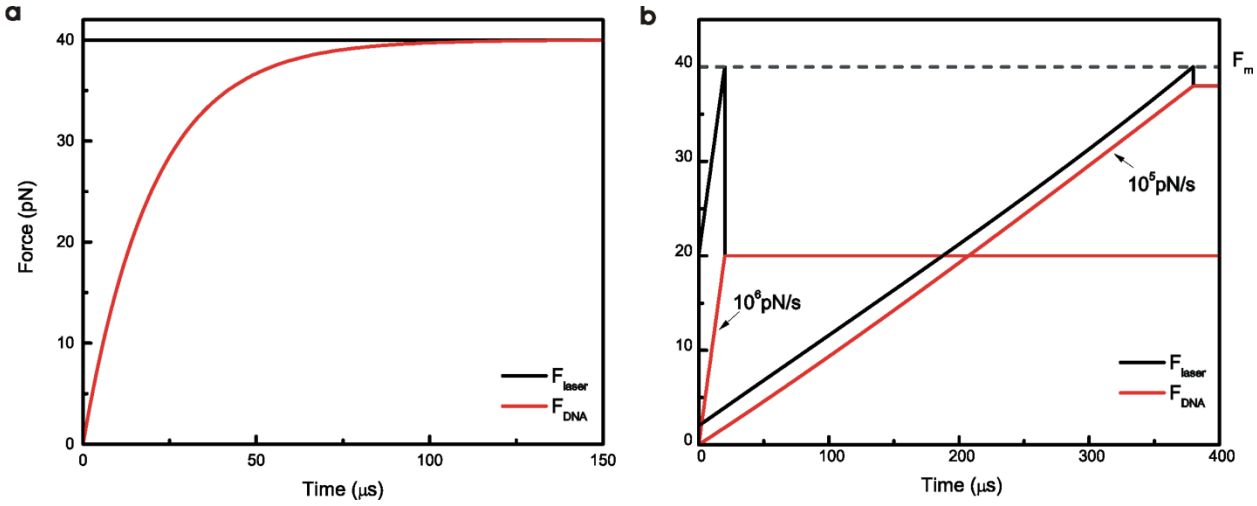

Supplementary Figure 9 | ***a.*** *Force response on the DNA ($L_c = 400nm$) if 40pN is applied instantaneously on the microsphere ($\phi\, 4.26\mu m$). The response time of the system is ~ 100μs.* ***b.*** *It is possible to achieve a linear force response on the DNA if an initial offset is applied to the force ramp of the laser. Note that a higher ramp results in a lower maximum force on the DNA.*

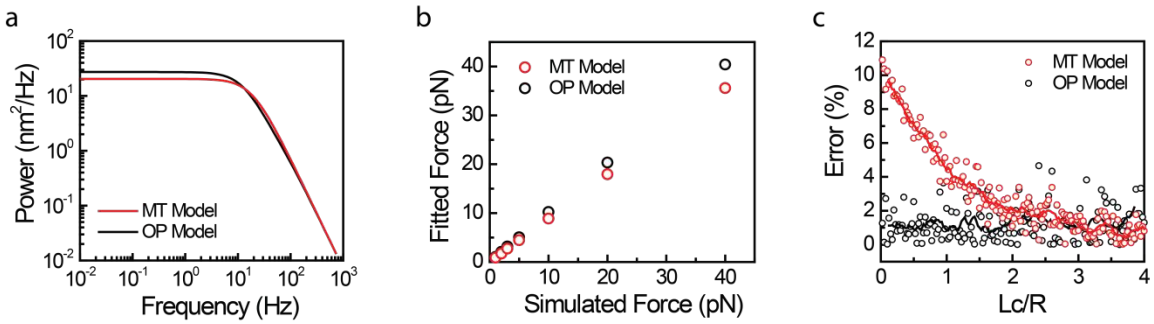

Supplementary Figure 10 | ***a.*** *Power spectra of the Magnetic Tweezer (MT) model (same as Velthuis et al mode in Supplementary Figure 3) and the Optical Pushing (OP) model (same as Sitters et al. model in Supplementary Figure 3) calculated for a microsphere that is 3 µm in diameter, a DNA with a contour length of 0.3 µm and a exerted force of 10 pN. The graph shows that the microspheres fluctuations are higher at lower frequencies if microsphere rotation is taken into account, leading to a higher plateau in the power spectrum for the OP case.* ***b.*** *Fitting power spectra of simulated data (acquired from trajectories of 600s) shows the MT model clearly underestimates the applied force, whereas the OP model predicts the forces accurately.* ***c.*** *The error of the fitted force (using 10pN) for simulated microsphere trajectories using the MT and the OP model. For microsphere-tether systems with* $L_c/R < 2$ *the OP model is clearly able to fit applied forces more accurately than the MT model.*

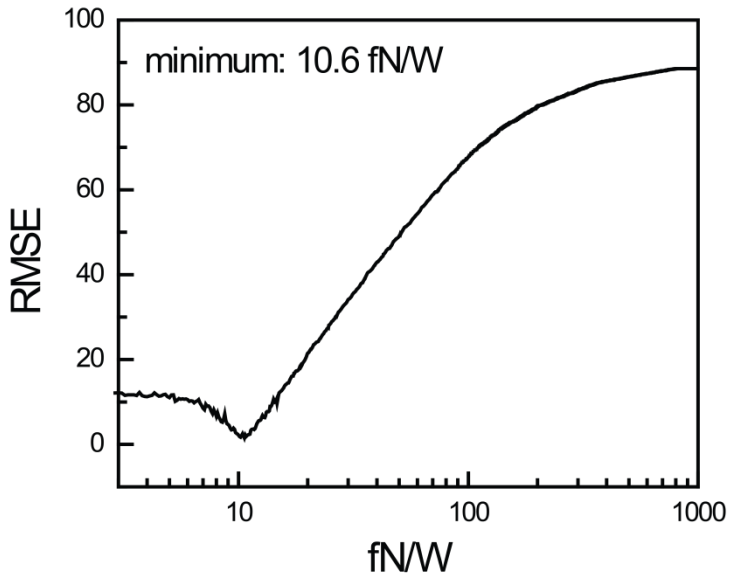

Supplementary Figure 11 | *The root mean squared error (RMSE) as a function of force calibration factor for the small beads (ϕ 440 nm). The minimum error corresponds to a calibration factor of 10.6 fN/W.*

(1) Te Velthuis, A. J. W.; Kerssemakers, J. W. J.; Lipfert, J.; Dekker, N. H. *Biophys. J.* **2010**, *99*, 1292–1302.

(2) Reif, F. *Fundamentals of statistical and thermal physics*; McGraw-Hill: Singapore, 1985.

(3) Howard, J. *Mechanics of motor proteins and the cytoskeleton*; 2001.

(4) Risken, H. *The Fokker-Plank Equation. Methods of Solution an Applications*; Springer Berlin Heidelberg: Berlin, 1989.

(5) Happel, J.; Brenner, H. *Low Reynolds Number Hydrodynamics*; Kluwer Academic Publishers: Dordrecht, The Netherlands, 1983.

(6) Marko, J. F.; Siggia, E. D. *Macromolecules* **1995**, *28*, 8759–8770.

(7) Schäffer, E.; Nørrelykke, S.; Howard, J. *Langmuir* **2007**, *287*, 3654–3665.

(8) *Absorption and Scattering of Light by Small Particles*; Bohren, C. F.; Huffman, D. R., Eds.; Wiley-VCH Verlag GmbH: Weinheim, Germany, 1998.

(9) Pawley, J. *Handbook of Biological Confocal Microscopy*; 3rd ed.; Springer Science + Business Media, 2006.

(10) Peterman, E. J. G.; Gittes, F.; Schmidt, C. F. *Biophys. J.* **2003**, *84*, 1308–1316.

(11) Segall, D.; Nelson, P.; Phillips, R. *Phys. Rev. Lett.* **2006**, *96*, 088306.